Control of lithospheric inheritance on neotectonic activity in northwestern Canada?

Pascal Audet, Christian Sole, and Andrew J. Schaeffer

Department of Earth and Environmental Sciences, University of Ottawa, Ottawa, Canada, K1N 6N5

ABSTRACT

Lithospheric inheritance is thought to affect the location and reactivation of tectonic structures through successive cycles of supercontinent formation and dispersal; however, its relation to neotectonic activity remains unclear. In northwestern Canada, abundant seismicity throughout the northern Canadian Cordillera (NCC) is geographically confined by several crustal-scale boundaries, yet its southern extent terminates abruptly along the inferred westward extension of a Late Cretaceous rifted margin boundary called the Liard Transfer Zone (LTZ). We use seismic data to show that the uppermost mantle beneath the Cordillera exhibits a sharp north-south contrast in fabric across the LTZ. South of the LTZ, fast axes of seismic wave propagation align closely with the lithospheric mantle fabric orientation of the adjacent Canadian Shield. North of the LTZ, fast axes reorient sub-parallel with the motion of the Pacific plate and follow the strike of the large dextral strike-slip Tintina and Denali faults. We attribute changes in anisotropic delay times across the Tintina and Denali faults to localized shear within the lithosphere, which implies that the crust and lithospheric mantle remained mechanically coupled during shearing. We propose that the contrast in uppermost mantle structure across the LTZ reflects a change in the nature and origin of the lithospheric mantle from inherited rifted margin structures, which affects the stability of the lithosphere and limits the extent of seismic activity

within the NCC. These results indicate that neotectonic activity in modern Cordilleras is controlled in part by inherited upper mantle structures.

INTRODUCTION

The Canadian Cordillera in western Canada is a wide, high-elevation, low relief orogenic plateau that initially formed as a passive margin in Late Proterozoic-earliest Cambrian as the result of the rifting of Laurentia, and underwent east-west compression in the Late Devonian (Monger and Price, 2002). The northern Canadian Cordillera (NCC) is bounded to the west by the Yakutat collision and the Alaskan border, to the east by the Proterozoic basement rocks of the Canadian Shield, and to the north by the Beaufort Sea (Fig. 1A). Its southern extension is not well defined but corresponds roughly with the southern limit of seismic activity, coinciding approximately with the Yukon-BC border at latitude 60° (Fig. 1A). This limit also follows the westward extension of the Liard Transfer Zone (LTZ) inherited from the asymmetric rifted margins of Laurentia that separated a lower plate (i.e., former foot wall) margin with seaward-dipping blocks to the north from an upper plate (i.e., former hanging wall) margin characterized by steep landward-dipping normal faults to the south (Cecile et al., 1997; Lund, 2008). The westernmost crustal portion south of the LTZ moved northwestward due to strike-slip motion along the Tintina Fault that produced approximately 450 km of right-lateral displacement (Hayward, 2015).

The NCC currently exhibits a high rate of tectonic deformation, mainly along its western portion around the Denali Fault and Yakutat collision zone, and across a broad zone to the north and east in the Richardson and Mackenzie Mountains, approximately 800 km east of the plate boundary (Fig. 1A; Leonard et al., 2008). The Tintina Fault generates only sparse, low magnitude seismicity and is mostly inactive due to unfavorable contemporary stress conditions

for strike-slip faulting (Maréchal et al., 2015). The current leading model to explain the high seismicity and rate of deformation far from the plate boundary proposes a thin and rigid crustal layer, decoupled from the underlying weak lower crust and mantle due to elevated basal temperatures, which is pushed horizontally at the plate boundary to the west by the oblique Yakutat collision and transmits stresses throughout the NCC (Mazzotti and Hyndman, 2002; Hyndman et al., 2005). According to this model, the sub-lithospheric upper mantle beneath the NCC is losing heat through vigorous and fluid-rich small-scale convection due to its recent position in a back arc setting (Hyndman and Currie, 2011). This model is supported by low values of effective elastic thickness (Audet et al., 2007) and high heat flow data across the NCC (Lewis et al., 2003) that require a thin and weak lithospheric mantle (~30 km) overlying a hot, homogeneous and convecting sub-lithospheric mantle. It is unclear, however, which factors control the geographical extent of seismicity within the Cordillera, in particular its southern boundary, without detailed regional information on the structure and properties of the crust and upper mantle.

UPPER MANTLE SEISMIC ANISOTROPY

Information on upper mantle structure can be obtained from estimates of seismic anisotropy (i.e., the directional dependence of seismic wave propagation speed), which is related to mineral fabrics that are generally acquired through shearing at high temperature via dislocation creep mechanisms, and reflect either dynamic mantle flow processes, or fossilized lithospheric fabric from past tectonic events (e.g., Long and Silver, 2009). Deciphering the source of anisotropy can lead to a better understanding of the role of the crust and upper mantle in controlling surface deformation. The source of upper mantle fabrics is generally attributed to the strain-induced alignment of the abundant mineral olivine generally characterized by

hexagonal symmetry (e.g., Nicolas and Christensen, 1987; Long and Silver, 2009). If the alignment of anisotropic olivine minerals is coherent over some depth range, it gives rise to observable seismic anisotropy. In particular, a singly polarized shear wave incident upon the anisotropic medium will split into two orthogonally polarized shear waves travelling at different wave speeds, a property commonly known as shear-wave splitting. Near-vertically propagating core-refracted, radially polarized shear waves (primarily SKS waves) are particularly sensitive to hexagonal anisotropy characterized by a horizontal axis of symmetry, enabling the study of lateral mantle flow or fossilized fabric. The splitting of SKS waves is parameterized by the accumulated delay time (δt) between the fast and slow shear waves that vary as a function of the intrinsic anisotropy and thickness of the anisotropic layer, and the azimuth (ϕ) of the fast axis of shear wave propagation (i.e., S1 polarization direction).

We collected seismic data from 12 broadband stations across the NCC in the Yukon and Northwest Territories, Canada, belonging to one of several seismic networks (Fig. 1B; Table DR1). Seismic data were processed to estimate teleseismic shear-wave splitting parameters using SKS phases (see Data Repository 201Xxxx). Single-station estimates were calculated from a vector average, with mean uncertainties of approximately 10° and 0.3 s for ϕ and δt, respectively. We also compiled published shear-wave splitting data for all stations located in northwestern Canada and southeastern Alaska. The final map of seismic anisotropy is shown in Figure 1B. The most striking feature is the large-scale, coherent NE-SW alignment of fast axis directions and large delay times (>1 sec) observed in the Canadian Shield. This pattern has been previously interpreted as a fossilized fabric within the thick (>150 km) lithospheric mantle of the North American continent and/or the sub-lithospheric mantle flow direction from the absolute motion

of the North American plate (Courtier et al. (2010); Snyder et al. (2007)) estimated from the MORVEL-NNR model (DeMets et al., 2010).

Within the Cordillera, the alignment of fast axes varies over short spatial scales. Toward the south and near the westward extension of the LTZ (Fig. 1B), fast axes are more closely aligned with those observed in the Canadian Shield, and may be due to either or both the extension of the North American fossilized fabric beneath the Cordillera, and the mantle flow direction due to absolute plate motion of North America. These results point to a possible influence of North American structure and/or dynamics on Cordilleran upper mantle fabric. To the north of the LTZ, we observe a noticeable change in the alignment of seismic fast axes. The northwestward, anti-clockwise rotation and margin-parallel alignment of the seismic fast axes (Fig. 1B, blue bars) were separately interpreted as the increasing influence of the Pacific-North America plate interactions 400 km from the plate boundary (Courtier et al., 2010), and fabric from the deep transpressive shear zone of the Denali Fault (Rasendra et al., 2014), respectively. The new data set (Fig. 1B, red bars) resolves a coherent alignment of seismic fast axes parallel to both the strike direction of the Tintina Fault, >200 km further away from the plate boundary, and the absolute motion of the Pacific plate. The spatial pattern of seismic fast axes north of the inferred LTZ suggests that upper mantle anisotropy may be related to sub-lithospheric mantle flow beneath the NCC induced by Pacific plate motion, and/or fossilized fabric associated with the two large crustal faults, which would require mantle penetrating shear zones.

SHEAR ZONE FABRICS

To investigate the influence of the Denali and Tintina faults on upper mantle anisotropy, we extract splitting parameters along two profiles oriented perpendicular to the strike of the Tintina Fault (Fig. 1B). Profile X-X' is located along the inferred extension of the LTZ, whereas

114 profile Y-Y' is located ~400 km to the northwest of the LTZ. The results are shown in Figure 2.
115 Along profile X-X', the azimuth of the seismic fast axes reflects a close alignment with the
116 fabric observed within the North American plate, and a consistent ~30° angle difference with the
117 absolute motion of North America (Fig. 2A). Azimuths rotate anti-clockwise toward the western
118 part of the profile (Fig. 1B, 2B), indicating a rotation of upper mantle fabric across a short
119 distance (~50 km), as outlined previously. More significantly, the delay times decrease from 1
120 sec to almost no splitting within 100 km of the surface trace of the Tintina Fault (Fig. 2B). The
121 absence of splitting near the fault may suggest that it did not generate measurable large-scale
122 coherent strain in the upper mantle, which we find unlikely. Alternatively, we posit that the
123 decrease in delay times is caused by the erasure of pre-existing North American fossilized fabric
124 by prolonged orthogonal (NW-SE) shearing along the Tintina Fault, which may randomize or
125 reduce fabrics and produce no observable splitting. The role of the Tintina Fault in controlling
126 upper mantle fabric is supported by splitting estimates along profile Y-Y', where the azimuths
127 are well aligned with the strike of the two large crustal faults (Fig. 2C). More importantly, delay
128 times increase from ~0.5 sec to >1.5 sec over a similar distance of 100 km to both the Denali and
129 Tintina faults (Fig. 2D). Results from both profiles suggest that up to 0.75-1 sec of accumulated
130 delay time may be due to fossilized fabric within the lithospheric mantle shear zones, with the
131 remainder possibly attributed to coherent, sub-lithospheric mantle flow. Assuming a negligible
132 contribution from crustal fabric, uniform shearing within a 30 to 50 km thick lithospheric mantle
133 with shear wave speed of 4.3 km/s producing 0.75-1 sec of anisotropic delay time amounts to 4-
134 11% of shear-zone related anisotropy, similar to values observed along the Alpine Fault in New
135 Zealand (Zietlow et al., 2014) and other large transcurrent faults (Vauchez et al., 2012).

These results imply that the crust and lithospheric mantle were mechanically coupled through at least part of the Paleogene to Mid-Neogene, when ~1000 km of dextral strike-slip displacement was distributed across a network of faults, the largest of which (the Denali and Tintina faults) accumulated >400 km of dextral motion (Johnston, 2008; Rasendra et al., 2015). North of the LTZ, the spatial coincidence of maximum anisotropic delay times with the surface trace of the faults further suggest that the hypothesized lower crustal detachment (Mazzotti and Hyndman, 2002) cannot have produced more than ~20 km of fault-perpendicular displacement of the upper crust relative to a weak lower crust and lithospheric mantle. This implies a maximum rate of horizontal displacement of ~1 mm yr^{-1} through the Miocene consistent with contemporaneous estimates from GPS data (Maréchal et al., 2015), but much lower than previous estimates of 5 mm yr^{-1} (Mazzotti and Hyndman, 2002). Finally, the bulk of seismic anisotropy beneath the NCC appears to be related to fossil fabric from lithospheric mantle shear zones, which leaves only a small possible contribution from coherent sub-lithospheric mantle flow.

INHERITANCE AND NEOTECTONICS

The contrast in seismic anisotropy across the LTZ indicates a north-south step change in the properties of the upper mantle in the Cordillera. One possible explanation for the change in anisotropy is the thermally controlled glide in olivine that switches slip system at temperatures <1000°C (Durham and Goetze, 1977; see also Dumouchy et al., 2013). However, this low-temperature transition is generally restricted to mylonites that accommodate the emplacement of peridotite slices in the crust (Vauchez et al., 1998). Furthermore, upper mantle temperatures are on average higher than 1000°C within the Cordilleran lithospheric mantle (Lewis et al., 2003). Instead, we propose that the change in seismic anisotropy represents a lateral transition in the

159 nature and origin of the lithospheric mantle fabric, which reflects a similar transition in the style
160 of rifting of the Late-Proterozoic Laurentian margin and coincides with a contrast in neotectonic
161 activity in the Cordillera (Fig. 3)

162 South of the LTZ, the preserved passive margin structures of the Cordillera are
163 characteristics of a former hanging wall margin formed by rifting on continent-ward dipping
164 listric normal faults (Fig. 3A,B). Seismic anisotropy results suggest that the inherited lithospheric
165 mantle of the former Laurentian margin underlies the Cordilleran crust south of the LTZ (Fig.
166 3C). North of the LTZ, the preserved passive margin structures of the NCC are characteristics of
167 a former foot wall margin with a broad sedimentary basin (Fig. 3A). In this region, the signature
168 of North American fossil fabric is absent, indicating that the upper mantle beneath the NCC has a
169 different origin. Instead, seismic anisotropy results indicate fabrics related to shearing along
170 mantle-penetrating shear zones. The nature of the upper mantle beneath the NCC is unclear and
171 could reflect material of a different origin (e.g., from terrane accretion), or the thermal erosion,
172 rejuvenation, or delamination of former North American lithospheric mantle (e.g., Bao et al.,
173 2014), or else the tectonic and/or magmatic underplating beneath the NCC during convergence
174 and plateau uplift.

175 Current seismic activity throughout the NCC may be partly the result of the oblique
176 collision of the Yakutat block; however, the long-term crust-mantle coupling beneath the
177 transpressive faults within the NCC, as well as the low inferred displacement rate, suggest that
178 stress may be transmitted, at least in part, by a process complementary to the lower-crustal
179 detachment model (e.g., basal tractions; Finzel et al. (2015)). Regardless of the origin of
180 neotectonic activity, its lateral extent is confined by large-scale lithospheric boundaries. The
181 inferred preservation of North American lithospheric mantle beneath the Cordillera south of the

LTZ suggests that the lithosphere remained relatively intact through plate convergence and transpression since the Late Cretaceous that affected the entire Canadian Cordillera (Johnston, 2008). The long-term stability of the upper mantle lithosphere may provide a backstop for neotectonic activity and control the extent of crustal deformation within the NCC. This interpretation is consistent with the presence of large lower crustal mafic bodies that juxtapose Cordilleran re-entrants (e.g., south of the LTZ), indicating a stronger lithosphere that forms buttresses against active deformation (Saltus and Hudson, 2007). Finally, the olivine LPO fabric may further induce large-scale mechanical anisotropy of the lithosphere, resulting in lateral contrasts in the strength of the lithosphere in the contemporary stress field that concentrate deformation perpendicular to the greatest strength directions (Audet and Bürgmann, 2011; Vauchez et al., 1998).

ACKNOWLEDGMENTS

We thank A. Vauchez, S. Mazzotti and an anonymous reviewer for their insightful comments. We also wish to thank the various federal, territorial and municipal agencies in the Yukon and Northwest Territories (YT Highway and Public Works, YT Energy Mines and Resources, Town of Faro, Town of Norman Wells, BC Wildfire Department, NT Environment and Natural Resources, and Nav Canada) for allowing us access to their land in the installation of the Yukon-Northwest Seismograph Network. This work is supported by the Natural Science and Engineering Research Council (Canada) through a Discovery Grant to PA and a Postdoctoral Fellowship to AJS, and by the Ministry of Research and Innovation of Ontario.

REFERENCES CITED

Audet, P., and Bürgmann, R., 2011, Dominant role of tectonic inheritance in supercontinent cycles: Nat. Geo., v. 4, p. 184-187.

205 Audet, P., Jellinek, A. M., and Uno, H., 2007, Mechanical controls on the deformation of
206 continents at convergent margins: Earth Planet. Sci. Lett., v. 264, p. 151-166.
207 Bao, X., Eaton, D. W., and Guest, B., 2014, Plateau uplift in western Canada caused by
208 lithospheric delamination along a craton edge: Nat. Geo., v. 7, p. 830-833.
209 Cecile, M. P., Morrow, D. W., and Williams, G. K., 1997, Early Paleozoic (Cambrian to Early
210 Devonian) tectonic framework, Canadian Cordillera: Bull. Can. Petrol. Geol., v. 45, p. 54-
211 74.
212 Courtier, A. M., Gaherty, J. B., Revenaugh, J., Bostock, M. G., and Garnero, E. J., 2010, Seismic
213 anisotropy associated with continental lithosphere accretion beneath the CANOE array,
214 northwestern Canada: Geology, v. 38, p. 887-890.
215 DeMets, C., Gordon, R. G., and Argus, D. F., 2010, Geologically current plate motions:
216 Geophys. J. Int., v. 181, p. 1-80, doi: 10.1111/j.1365-246X.2009.04491.x
217 Dumouchy, S., Tommasi, A., Ballaran, T. B., and Cordier, P., 2013, Low strength of Earth's
218 uppermost mantle inferred from tri-axial deformation experiments on dry olivine crystals,
219 Phys. Earth Planet. Int., v. 220, p. 37-49.
220 Durham, W. B., and Goetze, G., 1977, Plastic flow of oriented single crystals of olivine, 1.
221 Mechanical data: J. Geophys. Res., v. 82, p. 5737–5753.
222 Finzel, E. S., Flesch, L. M., Ridgway, K. D., Holt, W. E., and Ghosh, A., 2015, Surface motions
223 and intraplate continental deformation in Alaska driven by mantle flow: Geophys. Res. Lett.,
224 v. 42, p. 4350-4358.
225 Hayward, N., 2015, Geophysical investigation and reconstruction of lithospheric structure and its
226 control on geology, structure and mineralization in the Cordillera of northern Canada and
227 eastern Alaska: Tectonics, v. 34, p. 2165-2189.

Hyndman, R. D., Flück, P., Mazzotti, S., Lewis, T. J., Ristau, J., and Leonard, L., 2005, Current tectonics of the northern Canadian Cordillera: Can. J. Earth Sci., v. 42, p. 1117-1136.

Hyndman, R. D., and Currie, C.A., 2011, Why is the North America Cordillera high? Hot backarcs, thermal isostasy, and mountain belts: Geology, v. 39, no. 8, p. 783-786.

Johnston, S. T., 2008, The Cordilleran ribbon continent of North America: Annu. Rev. Earth Planet. Sci., v. 36, p. 495-530.

Leonard, J. L., Mazzotti, S., and Hyndman, R. D., 2008, Deformation rates estimated from earthquakes in the northern Cordillera and eastern Alaska: J. Geophys. Res., v. 113, p. B08406.

Lewis, T. J., Hyndman, R. D., and Flück, P., 2003, Heat flow, heat generation, and crustal temperatures in the northern Canadian Cordillera: Thermal control of tectonics: J. Geophys. Res., v. 108, no. B6, 2316.

Long, M. D., and Silver, P. G., 2009, Shear wave splitting and mantle anisotropy: Measurements, interpretations, and new directions: Surv. Geophys., v. 30, p. 407-461.

Lund, K., 2007, Geometry of the Neoproterozoic and Paleozoic rift margin of western Laurentia: Implications for mineral deposit settings: Geosphere: v. 4, no. 2, p. 429-444.

Maréchal, A., Mazzotti, S., Elliott, J. L., Freymueller, J. T., and Schmidt, M., 2015, Indentor-corner tectonics in the Yakutat-St. Elias collision constrained by GPS: J. Geophys. Res., v., 120, p. 3897–3908.

Mazzotti, S., & Hyndman, R. D., 2002, Yakutat collision and strain transfer across the northern Canadian Cordillera: Geology, v. 30, p. 495-498.

Monger, J., and Price, R., 2002, The Canadian Cordillera: Geology and tectonic evolution: CSEG Recorder, v. 27, p. 17-36.

Nicolas, A., and N. I. Christensen, 1987, Formation of anisotropy in upper mantle peridotites—a review, in *The Composition, Structure and Dynamics of the Lithosphere-Asthenosphere System, American Geophysical Union Geodynamics Series,* edited by C. Froidevaux and K. Fuchs, pp. 111-123.

Rasendra, N., Bonnin, M. Mazzotti, S., and Tiberi, C., 2014, Crustal and upper-mantle anisotropy related to fossilized transpression fabric along the Denali Fault, northern Canadian Cordillera: Bull. Seism. Soc. Am., v. 104, p. 1964-1975.

Saltus, R. W., and Hudson, T. L., 2007, Regional magnetic anomalies, crustal strength, and the location of the northern Cordilleran fold-and-thrust belt: Geology, v. 35, no. 6, p. 567-570.

Snyder, D., and Bruneton, M., 2007, Seismic anisotropy of the Slave craton, NW Canada, from joint interpretation of *SKS* and Rayleigh waves: Geophys. J. Int., v. 169, p. 170-188.

Vauchez, A., Tommasi, A., and Barruol, G., 1998, Rheological heterogeneity, mechanical anisotropy and deformation of the continental lithosphere: Tectonophysics, v. 296, p. 61–86

Vauchez, A., Tommasi, A., and Mainprice, D., 2012, Faults (shear zones) in the Earth's mantle: Tectonophysics, v. 558-559, p. 1-27.

Zietlow, D. W., Sheehan, A. F., Molnar, P. H., Savage, M. K., Hirth, G., Collins, J. A., and Hager, B. H., 2014, Upper mantle seismic anisotropy at a strike-slip boundary: South Island, New Zealand: J. Geophys. Res., v. 119, p. 1020-1040.

FIGURE CAPTIONS

Figure 1. **A**. Map of northwestern Canada. Grey dots show earthquakes that occurred between 2000 and 2016. Thick white lines indicate tectonic boundaries separating the northern Canadian Cordillera (NCC) from the adjacent Canadian Shield (CS). AB: Alberta; AK: Alaska; BC:

British Columbia; NT: Northwest Territories; NU: Nunavut; YK: Yukon. The Liard Transfer Zone (Liard TZ) is shown as white dashed lines. **B**. Multi-event average results of teleseismic shear-wave splitting. Blue and red bars with white symbols show the orientation of the seismic fast axes and the accumulated delay time between the fast and slow shear waves for each station in the compiled data set (blue) and from this study (red). Compiled data are from Courtier et al., (2010), Rasendra et al. (2014), and Snyder et al. (2007). Square and triangular symbols show stations for which the splitting parameters are projected along lines X-X' and Y-Y', respectively, and shown in Figure 2. Large white arrows with labels show the absolute plate motion directions of North America (NA) and Pacific (PAC) plates, according to the no-net rotation frame model of DeMets et al., 2010.

Figure 2. Multi-event station average ϕ (**A**, **C**) and δt (**B**, **D**) along the X-X' (**A**, **B**) and Y-Y' (**C**, **D**) profiles perpendicular to the Tintina Fault (dotted vertical line at distance of 0 km) shown in Figure 1B. Thick solid lines show the average absolute plate motion of the North American (NA) and Pacific (PAC) plates from the MORVEL model (DeMets et al., 2010). The horizontal black dashed line in **A** and **C** shows the strike of the Tintina Fault along both profiles.

Figure 3. **A**. Late Proterozoic-Early Cambrian rifted margin of Laurentia showing a south-to-north transition from an upper plate margin to a lower plate margin along the Liard Transfer Zone. **B**. Schematic style of faulting along the asymmetric rifted margin and across the LTZ. **C**. Contemporary tectonic setting in northwestern Canada, showing the inferred location of North American upper mantle underlying the Cordilleran crust south of the LTZ in relation with neotectonic activity (shown by earthquakes). Figure modified from Lund (2008).

[1]GSA Data Repository item 201Xxxx, describing the methodology for single-event teleseismic SKS splitting, two figures with example results and two tables with compiled estimates**,** is available online at www.geosociety.org/pubs/ft20XX.htm, or on request from editing@geosociety.org or Documents Secretary, GSA, P.O. Box 9140, Boulder, CO 80301, USA.

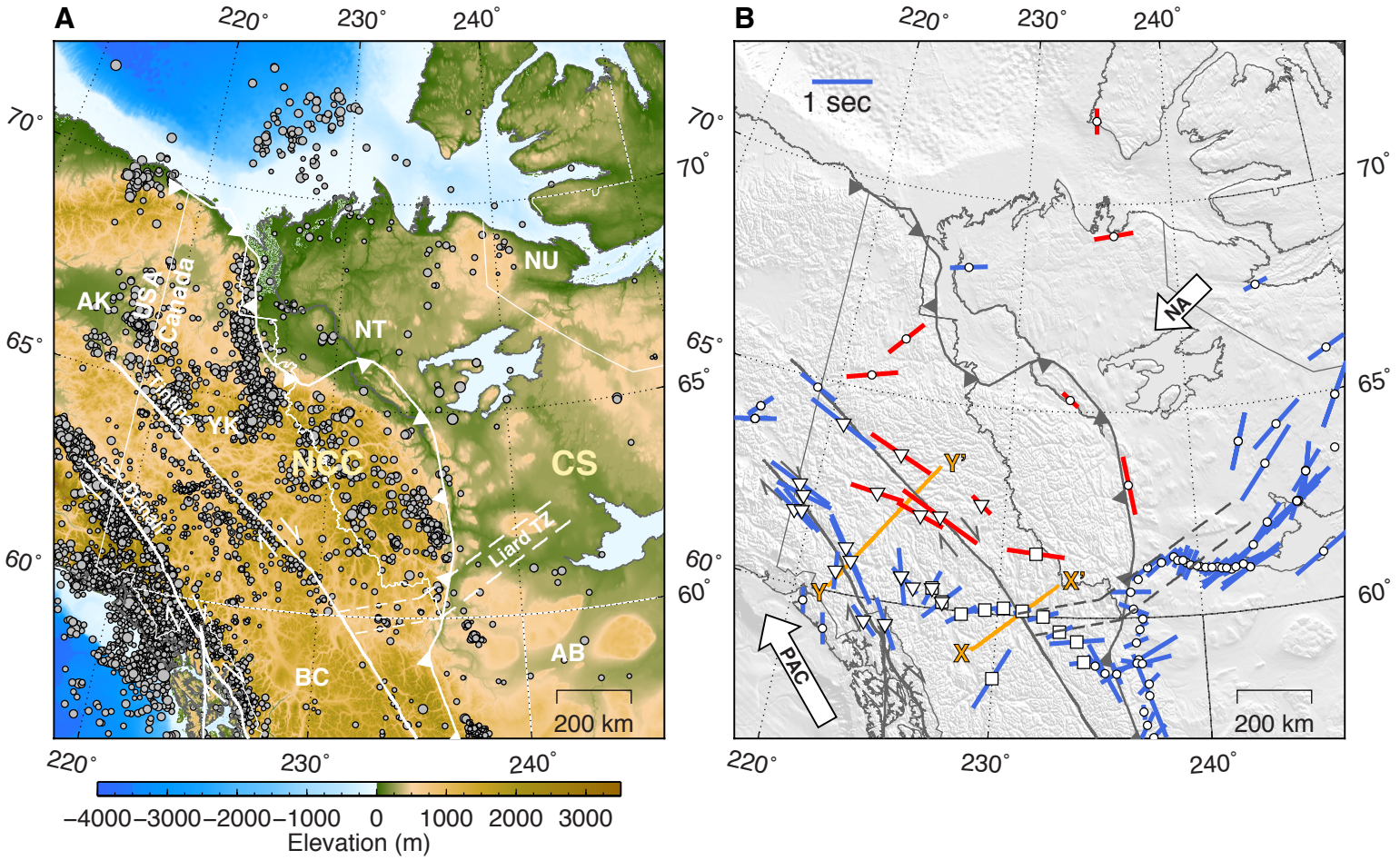
A
B
220°
230°
240°
70°
65°
60°
AK
USA
Canada
NT
NU
CS
AB
BC
Liard TZ
Denali
Fairweather
Queen Charlotte
1 sec
NA
PAC
Y'
Y
X'
X
200 km
−4000 −3000 −2000 −1000 0 1000 2000 3000
Elevation (m)

Figure 1

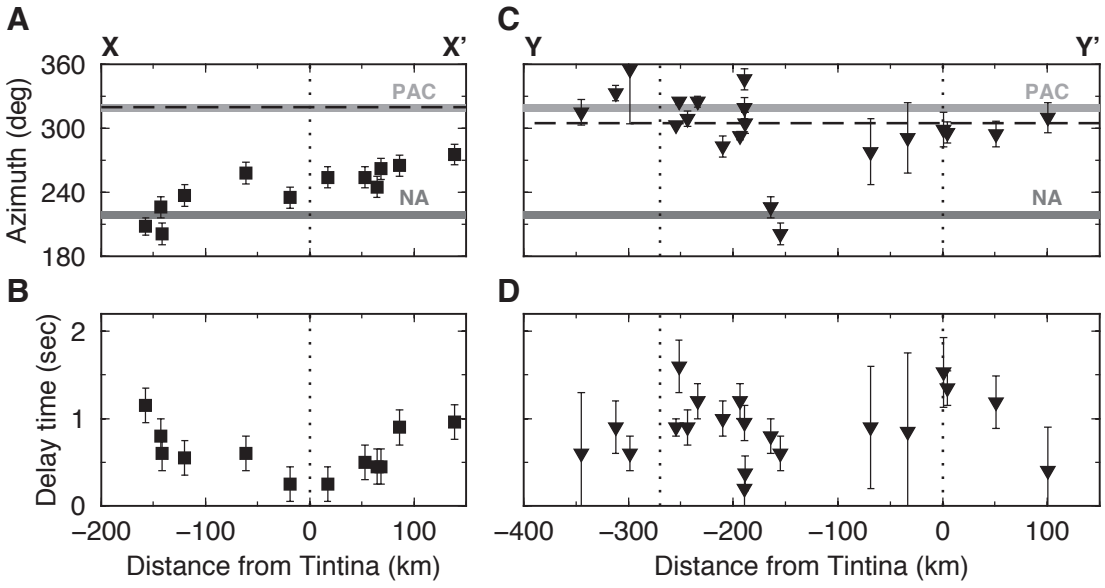
A
X
X'
360
300
240
180
Azimuth (deg)
PAC
NA
C
Y
Y'
PAC
NA
B
Delay time (sec)
2
1
0
–200
–100
0
100
Distance from Tintina (km)
D
–400
–300
–200
–100
0
100
Distance from Tintina (km)

Figure 2

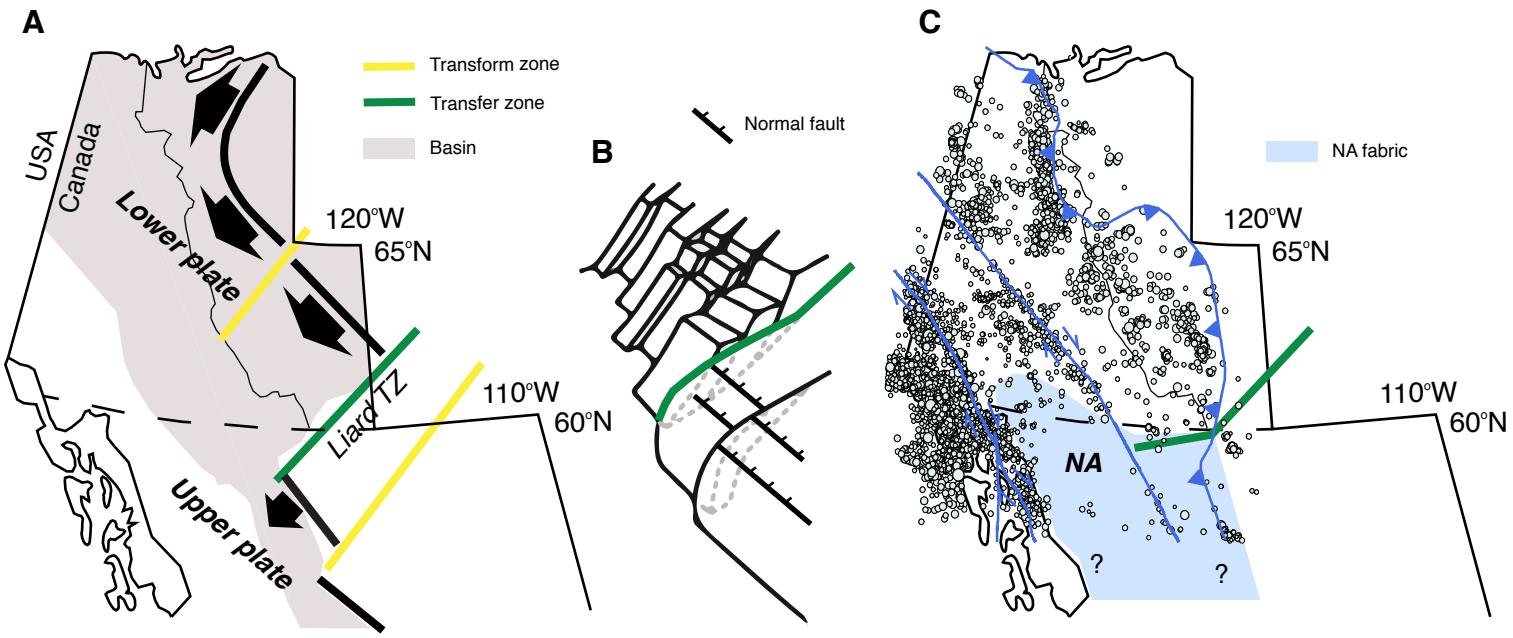
A
Transform zone
Transfer zone
Basin
USA
Canada
Lower plate
120°W
65°N
Liard TZ
110°W
60°N
Upper plate
B
Normal fault
C
NA fabric
120°W
65°N
110°W
60°N
NA
?
?

Figure 3

GSA DATA REPOSITORY 201Xxxx

Control of lithospheric inheritance on neotectonic activity in northwestern Canada?

Pascal Audet, Christian Sole, and Andrew J. Schaeffer

Department of Earth and Environmental Sciences, University of Ottawa, Ottawa, Canada, K1N 6N5

TELESEISMIC SHEAR-WAVE SPLITTING ANALYSIS

Upon entering an anisotropic medium characterized by azimuthal anisotropy, upgoing radially-polarized and planar SKS waves will split into two orthogonal components, one of which will travel along the fast axis of seismic propagation (with azimuth ϕ), whereas the other component will travel along the perpendicular slow axis. Depending on the thickness of the medium and wave speed difference between the fast and slow axis of hexagonal symmetry, a delay time δt will accumulate between the two polarized shear waves. The splitting process is thus completely characterized by the parameters ϕ and δt (Silver, 1996). Incidentally, shear waves initially travelling along one of the symmetry axes will not produce any observable splitting. These results are called "null" measurements and can further help to constrain the orientation ϕ. Anisotropy that varies with depth or described by a different class of symmetry (or hexagonal anisotropy with a dipping axis of symmetry) will give rise to more complicated patterns of splitting.

We used 6 stations from the Transportable Array of USArray (TA), 5 stations from the Yukon-Northwest Seismograph Network (NY), and one station from the Polaris Network (PO)

(Table DR1). We selected waveforms for all magnitude M>6.0 events with signal-to-noise ratio greater than 4 dB in the epicentral distance range of 85-140° that occurred between April 2014 and March 2016. Waveforms are rotated into a longitudinal-radial-tangential (LQT) coordinate system and filtered using a 0.05-0.15 Hz band-pass filter (Currie et al., 2004). Shear wave splitting analysis at each station was carried out using the SplitLab software (Wüstefeld et al., 2008) and resulted in 61 successful (i.e. non-null, see below) splitting measurements from SKS phases (Tables DR1 and DR2). The number of estimates is low for recently installed stations of the TA network. SplitLab performs the splitting analysis based on two distinct methods. The energy minimization method (also called SC method) (Silver and Chan, 1991) seeks the splitting parameters ϕ and δt for which the energy of the transverse shear wave component is minimized after inverting the splitting process. In contrast, the rotation-correlation method (also called the RC method) rotates the seismogram of interest into a test coordinate frame and searches for the pair of splitting parameters that gives the maximum cross correlation between the transverse and radial SKS components (Wüstefeld et al., 2008).

Results are first classified into nulls if they satisfy two criteria: 1) SNR of the tangential component of the SKS phase is below 3 dB, or 2) the difference in ϕ obtained from the SC and RC methods is between 22 and 68 degrees (Wüstefeld and Bokelmann, 2007). Both nulls and non-nulls are then qualitatively evaluated in terms of "Good", "Fair" and "Poor" results based on the ratio of RC and SC delay times ($\rho = \delta t_{RC}/\delta t_S$) and the difference between RC and SC azimuths ($\delta\phi = \max[|\phi_{RC}-\phi_{SC}|, |\phi_{SC}-\phi_{RC}|]$) (Wüstefeld and Bokelmann, 2007). For Nulls, these correspond to $\rho < 0.2$, $37° < \delta\phi < 53°$ for “Good” measurements; $\rho < 0.3$, $32° < \delta\phi < 58°$ for “Fair”; and “Poor” otherwise. For non-Nulls, these correspond to $0.8 < \rho < 1.1$, $\delta\phi < 8°$ for

"Good" measurements; $0.7 < \rho < 1.2$, $\delta\phi < 15°$ for "Fair"; and "Poor" otherwise. Parameter uncertainty was estimated from the 95% confidence interval using an F-test (Walsh et al., 2013).

An example result of parameter estimation for a single event recorded at station EPYK is shown in Figure DR1. Figure DR2 shows the compilation of "good" and "fair", non-null results for station EPYK, sorted by back-azimuth of incoming SKS waves. These results show tightly clustered estimates of both ϕ and δt, and we interpret these in terms of a single layer with horizontal anisotropy. We note, however, that the event distribution is not uniform in back-azimuth, and the single-layer assumption may not hold in reality. We then separately perform a vector average of all "good" and "fair" non-null results (weighting the estimates equally) for both the SC and RC techniques, and obtain final estimates by vector averaging the results of both techniques into a single estimate of ϕ and δt for each station (Table DR1), further preventing us from considering more complex (i.e., multi-layered or dipping) anisotropy models. We also ignore covariance and our error estimates are likely lower bounds. Figure DR3A shows all 'fair' and 'good' measurements at each station.

Null estimates can also provide qualitative information on the robustness of the splitting parameters. Null measurements occur because: 1) there is no detectable anisotropy beneath the station; or 2) the incoming SKS wave propagates along either the slow or fast axis of anisotropy. We plot the back-azimuth of all "good" null measurements as rose diagrams in Figure DR3B, along with the estimated splitting parameters (reproduced from Figure 1B). Each set of measurements is binned in 10° back-azimuth and the length of the bars is proportional to the percent number of measurements in each bin. These results show that the dominant back-azimuths of "null" measurements are aligned with either the fast axis or perpendicular to it, thus qualitatively confirming that the splitting measurements are robust.

NOTES

The SplitLab software used in this study was translated from Matlab® to Python and thoroughly tested against published results. The Python software makes extensive use of the ObsPy module developed by Beyreuther et al. (2010), and is available upon request.

REFERENCES CITED

Beyreuther, R. Barsch, L. Krischer, T. Megies, Y. Behr and J. Wassermann, 2010, ObsPy: A Python Toolbox for Seismology: Seism. Res. Lett., v. 81, no. 3, p. 530-533.

Currie, C. A., Cassidy, J. F., Hyndman, R. D., and Bostock, M. G., 2004, Shear wave anisotropy beneath the Cascadia subduction zone and western North American Craton: Geophys. J. Int., v. 157, p. 341–353.

Silver, P. G., 1996, Seismic anisotropy beneath the continents: Probing the depths of geology: Annu. Rev. Earth Planet. Sci., v. 24, p. 385-432.

Silver, P. G., and Chan, W. W., 1991, Shear-wave splitting and subcontinental mantle deformation: J. Geophys. Res., v. 96, p. 429-454.

Walsh, E., Arnold, R., and Savage, M. K., 2013, Silver and Chan revisited: J. Geophys. Res., v. 118, p. 5500-5515.

Wüstefeld, A., and Bokelmann, G., 2007, Null detection in shear-wave splitting measurements: Bull. Seism. Soc. Am., v. 97, no. 4, p. 1204-1211.

Wüstefeld, A., Bokelmann, G., Zaroli, C., and Barruol, G., SplitLab: A shear-wave splitting environment in Matlab: Comp. Geosci.

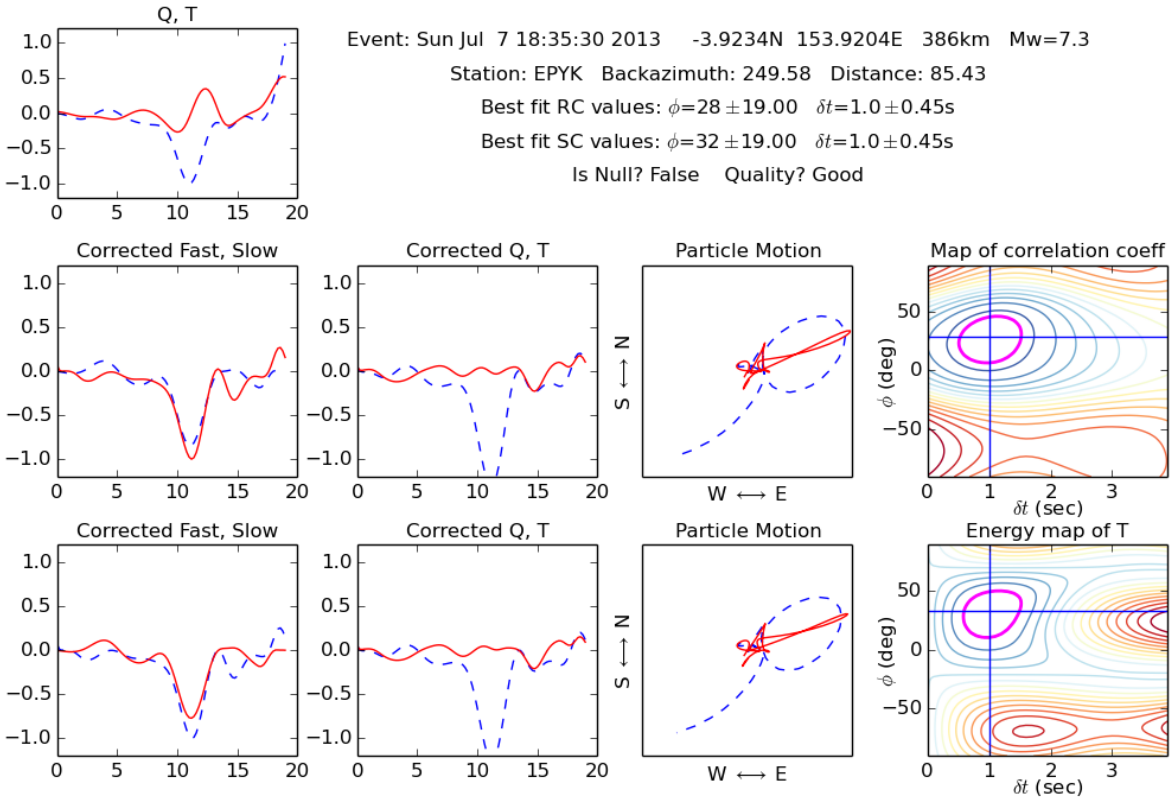

Figure DR1. Example result of a single-event estimate of SKS splitting obtained at station EPYK. The text describes the earthquake parameters and best-fit estimates for both the RC and SC techniques, as well as the quality factor. The top left panel shows the longitudinal (Q, blue) and tangential (T, red) seismograms for a hand picked window around the predicted SKS phase arrival. The bottom two rows of panels show inversion results for the RC (middle row) and SC (bottom row) techniques. For each technique, the first two panels represent the fast (blue) and slow (red) components and the longitudinal (blue) and tangential (red) components after removing the effect of splitting. Horizontal axis is time in seconds. The last two panels show the initial (blue) and corrected (red) particle motion in the horizontal plane, and the misfit contours (low misfit in blue, high misfit in red), shown either as a map of the correlation coefficient between the corrected fast and slow components (RC) or the energy of the tangential component after correction. The magenta contours show the 95% confidence interval.

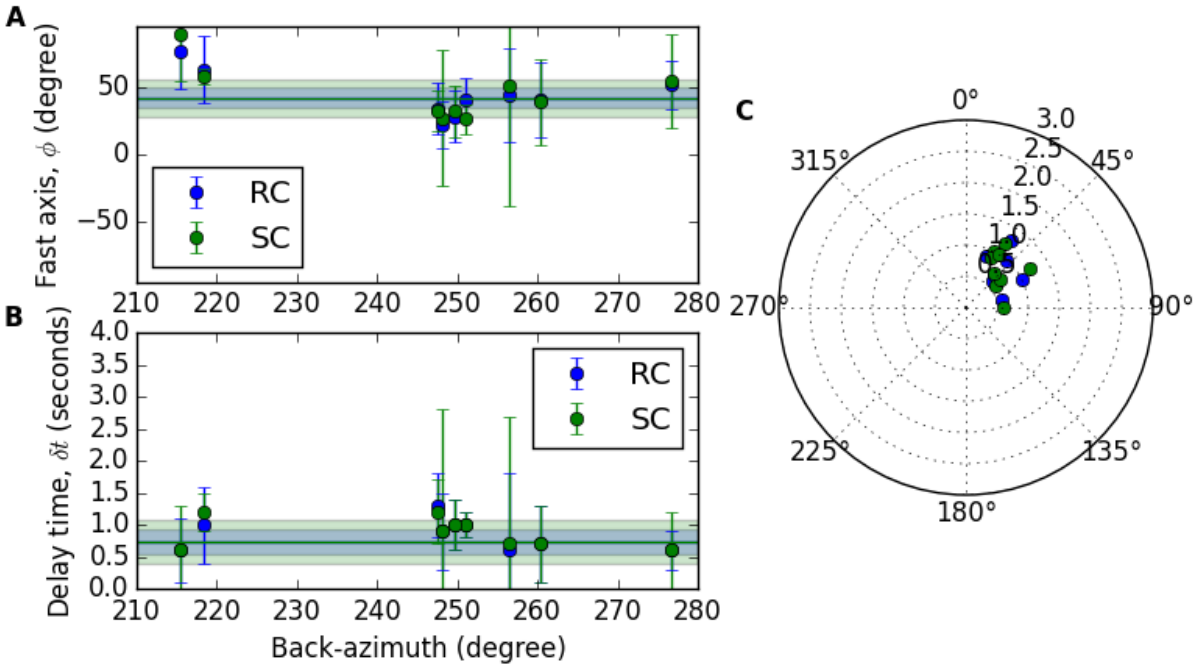

Figure DR2. Compilation of SKS splitting results for all "Good" and "Fair" non-nulls for station EPYK. **A**: Azimuth of fast shear-wave propagation; **B**: Delay time between fast and slow shear waves. Blue and Green symbols represent results obtained from the RC and SC techniques, respectively. The blue and green shaded areas show the standard deviation of each quantity around the mean value (solid lines) obtained from a vector average of individual measurements. **C**: Representation of the estimated azimuths and delay times as a polar plot with delay time increasing radially from the origin, which emphasizes the clustering of splitting parameters.

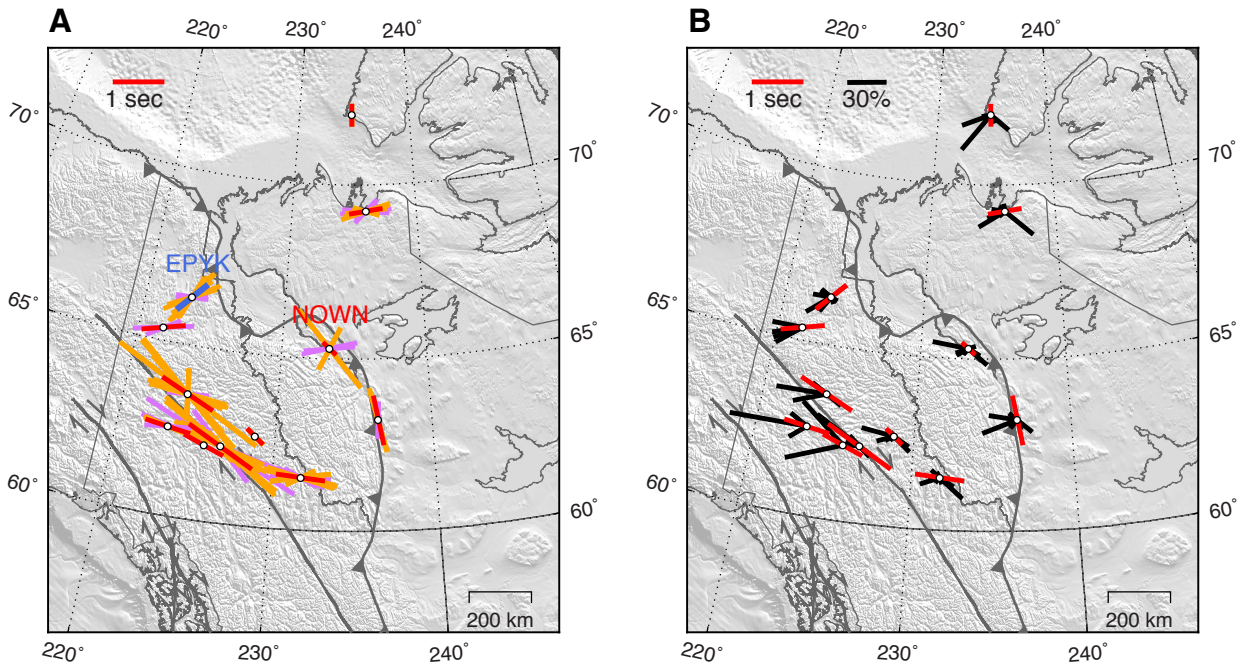

Figure DR3. **A**. Map of SKS splitting results for all "fair" and "good" non-nulls shown as purple and orange bars, respectively. Except for station NOWN that displays variable fast axis directions perhaps indicative of multi-layered anisotropy, all stations show a tight distribution around the average parameters shown in red. Station EPYK is highlighted in blue. **B**. Map of null measurements for all "good" nulls plotted as rose diagrams (black bars) of back-azimuths of incoming SKS waves. The bars represent the percent number of events per 10° back-azimuth bin. Estimated SKS splits appear in red (reproduced from Figure 1B) in both **A** and **B**.

Table DR1: Station average splitting parameters

Stations				RC Avg.				SC Avg.					Station Avg.			
Network	Name	Lon (°)	Lat (°)	ϕ (°)	σ_ϕ	δt (s)	$\sigma_{\delta t}$	ϕ (°)	σ_ϕ	δt (s)	$\sigma_{\delta t}$	#	ϕ (°)	σ_ϕ	δt (s)	$\sigma_{\delta t}$
TA	M31M	-134.391	62.202	-74.00	29.00	0.80	0.80	-64.00	37.00	0.90	1.00	1	-69.00	33.00	0.85	0.90
NY	MMPY	-131.262	62.619	-52.00	15.00	0.40	0.20	-48.00	41.00	0.40	0.90	1	-50.00	28.00	0.40	0.55
PO	NOWN	-126.715	65.294	-49.21	32.27	0.26	0.76	-47.09	32.64	0.35	0.73	3	-48.15	32.45	0.30	0.74
TA	I29M	-138.306	63.361	69.85	45.72	0.69	1.02	78.20	22.73	1.00	0.65	2	74.02	34.22	0.84	0.83
TA	A36M	-125.250	71.990	0.00	19.00	0.40	0.20	-1.00	38.00	0.40	0.60	1	-0.50	28.50	0.40	0.40
TA	C36M	-124.070	69.347	83.77	11.36	0.61	0.25	78.40	17.63	0.65	0.52	7	81.08	14.49	0.63	0.38
NY	WGLY	-123.458	63.228	-13.25	19.24	1.00	0.43	-8.12	20.94	0.96	0.46	2	-10.69	20.09	0.98	0.45
TA	M30M	-136.793	62.576	-77.44	45.21	0.90	1.02	-87.04	17.72	0.91	0.41	2	-82.24	31.47	0.90	0.72
NY	FARO	-133.348	62.230	-63.34	20.81	1.46	0.48	-59.07	12.86	1.60	0.41	9	-61.21	16.84	1.53	0.44
NY	MAYO	-135.892	63.596	-66.42	10.46	1.15	0.25	-64.26	14.26	1.23	0.35	14	-65.34	12.36	1.19	0.30
TA	EPYK	-136.719	66.370	41.96	7.91	0.74	0.20	41.52	13.49	0.73	0.34	9	41.74	10.70	0.73	0.27
NY	TGTN	-128.273	61.527	-84.05	10.83	0.95	0.19	-85.16	8.76	0.98	0.26	10	-84.61	9.80	0.96	0.22

Table DR2: Individual Station Splitting Parameters

	Event Info					RC				SC			
Station	Date	Lon (°)	Lat (°)	Mag	Φ (°)	ϕ (°)	σ_ϕ	δt (s)	$\sigma_{\delta t}$	ϕ (°)	σ_ϕ	δt (s)	$\sigma_{\delta t}$
A36M	8/24/14	-73.57	-14.60	6.8	130.4	0.00	19.00	0.40	0.20	-1.00	38.00	0.40	0.60
	5/24/15	-175.96	-19.39	6.2	-131.6	76.00	37.00	0.90	0.70	72.00	10.00	1.00	0.30
	4/17/15	-178.60	-15.88	6.5	-128.2	-85.00	33.00	0.90	0.70	85.00	32.00	1.00	0.80
	4/7/15	-173.22	-15.17	6.3	-133.0	84.00	19.00	0.80	0.40	83.00	28.00	0.80	0.50
C36M	11/26/14	126.58	1.96	6.8	-71.1	57.00	17.00	0.50	0.30	44.00	44.00	0.60	1.90
	5/21/14	88.04	18.20	6.0	-30.3	-73.00	33.00	0.50	0.70	-75.00	89.00	0.50	2.00
	5/15/14	122.06	9.38	6.3	-64.4	72.00	10.00	0.60	0.20	80.00	44.00	0.60	1.90
	11/23/13	-176.54	-17.12	6.5	-130.5	-88.00	45.00	0.60	1.10	78.00	39.00	0.70	1.00
	9/16/15	151.48	-6.01	6.1	-108.9	41.00	16.00	1.00	0.20	26.00	11.00	1.00	0.20
	12/7/14	154.46	-6.51	6.6	-111.9	22.00	17.00	0.90	0.60	27.00	51.00	0.90	1.90
	11/21/14	127.06	2.30	6.5	-83.3	52.00	18.00	0.60	0.30	54.00	35.00	0.60	0.60
	11/1/14	-177.76	-19.69	7.1	-141.7	63.00	25.00	1.00	0.60	58.00	6.00	1.20	0.30
EPYK	7/29/14	146.77	-3.42	6.0	-103.6	44.00	35.00	0.60	1.20	51.00	89.00	0.70	2.00
	5/7/14	154.90	-6.96	6.0	-112.5	34.00	19.00	1.30	0.50	32.00	15.00	1.20	0.50
	8/1/13	-173.50	-15.24	6.0	-144.5	77.00	29.00	0.60	0.50	89.00	35.00	0.60	0.70
	7/7/13	153.92	-3.92	7.3	-110.4	28.00	19.00	1.00	0.40	32.00	19.00	1.00	0.40
	4/16/13	142.54	-3.22	6.6	-99.7	40.00	28.00	0.70	0.60	39.00	32.00	0.70	0.60
	9/16/15	151.48	-6.01	6.1	-105.8	-57.00	89.00	0.40	2.00	-66.00	89.00	0.40	2.00

continued on next page

FARO

continued from previous page

	Event Info					RC				SC			
Station	Date	Lon (°)	Lat (°)	Mag	Φ (°)	ϕ (°)	σ_ϕ	δt (s)	$\sigma_{\delta t}$	ϕ (°)	σ_ϕ	δt (s)	$\sigma_{\delta t}$
	5/22/15	163.22	-11.11	6.8	-118.4	-55.00	13.00	3.00	0.70	-58.00	9.00	2.90	0.90
	5/22/15	163.70	-11.06	6.9	-118.9	-75.00	20.00	3.50	0.90	-64.00	13.00	3.60	0.80
	2/27/15	122.53	-7.30	7.0	-80.7	-45.00	31.00	0.70	0.90	-51.00	36.00	0.80	0.80
	11/15/14	126.52	1.89	7.1	-80.0	-53.00	89.00	1.10	2.00	-53.00	30.00	1.10	0.90
	11/1/14	-177.76	-19.69	7.1	-138.7	-71.00	30.00	1.70	1.10	-65.00	6.00	1.90	0.50
	10/9/14	-110.81	-32.11	7.0	160.9	-54.00	89.00	1.50	2.00	-44.00	27.00	1.80	1.40
	7/14/14	126.48	5.71	6.3	-78.2	-40.00	31.00	0.40	0.60	-37.00	47.00	0.40	1.90
	5/4/14	179.09	-24.61	6.6	-137.6	-74.00	89.00	1.90	1.80	-68.00	8.00	2.10	0.80
I29M	2/15/16	-175.48	-21.00	6.0	-145.6	81.00	21.00	0.80	0.40	80.00	29.00	0.80	0.50
	1/11/16	126.86	3.90	6.5	-83.9	57.00	89.00	0.70	2.00	77.00	35.00	1.20	1.20
M30M	4/13/16	94.90	23.13	6.9	-46.4	-77.00	89.00	1.00	2.00	-79.00	10.00	1.00	0.20
	10/20/15	167.30	-14.86	7.1	-126.7	-78.00	16.00	0.80	0.40	84.00	34.00	0.90	0.80
M31M	4/3/16	166.82	-14.35	6.9	-123.9	-74.00	29.00	0.80	0.80	-64.00	37.00	0.90	1.00
	10/20/15	167.30	-14.86	7.1	-125.9	-69.00	18.00	1.10	0.20	-62.00	7.00	1.20	0.20
	9/26/15	-71.32	-30.81	6.3	125.6	-8.00	31.00	1.00	1.00	-5.00	89.00	1.00	2.00
	9/21/15	-71.38	-31.73	6.6	126.1	89.00	23.00	0.70	0.70	-80.00	89.00	0.80	2.00
	5/22/15	163.22	-11.11	6.8	-120.8	-62.00	15.00	3.50	0.60	-62.00	10.00	3.50	0.80
	5/20/15	164.17	-10.88	6.8	-121.6	-51.00	16.00	2.10	0.80	-52.00	89.00	2.10	2.00
	5/7/15	154.56	-7.22	7.1	-111.4	-63.00	19.00	1.10	0.20	-64.00	14.00	1.10	0.20
MAYO	3/3/15	98.72	-0.78	6.1	-57.7	86.00	13.00	0.80	0.20	-85.00	19.00	0.90	0.40
	11/1/14	-177.76	-19.69	7.1	-141.0	-81.00	5.00	1.40	0.20	-76.00	4.00	1.50	0.20

continued on next page

continued from previous page

	Event Info					RC				SC			
Station	Date	Lon (°)	Lat (°)	Mag	Φ (°)	ϕ (°)	σ_ϕ	δt (s)	$\sigma_{\delta t}$	ϕ (°)	σ_ϕ	δt (s)	$\sigma_{\delta t}$
	10/9/14	-110.81	-32.11	7.0	158.7	-64.00	29.00	0.50	0.50	-73.00	37.00	0.50	0.70
	7/8/14	168.40	-17.69	6.2	-127.9	-83.00	24.00	1.10	0.50	-72.00	16.00	1.20	0.50
	5/4/14	178.24	-25.81	6.3	-139.3	-77.00	89.00	1.30	2.00	-79.00	89.00	1.30	2.00
	4/26/14	-174.71	-20.75	6.1	-144.0	-84.00	11.00	1.60	0.50	-80.00	19.00	1.70	1.10
	4/13/14	162.05	-11.46	7.4	-119.9	-81.00	35.00	0.60	0.90	-68.00	43.00	0.60	1.80
	4/12/14	155.24	-7.10	6.1	-111.9	-50.00	89.00	2.90	2.00	-48.00	60.00	2.90	1.50
MMPY	7/4/14	152.81	-6.23	6.5	-105.2	-52.00	15.00	0.40	0.20	-48.00	41.00	0.40	0.90
	4/7/15	-173.22	-15.17	6.3	-135.4	77.00	33.00	1.10	1.00	84.00	33.00	1.00	0.80
NOWN	12/7/14	154.46	-6.51	6.6	-102.7	27.00	19.00	0.90	0.40	26.00	24.00	0.90	0.40
	12/6/14	130.48	-6.11	6.0	-80.8	-40.00	89.00	2.00	2.00	-40.00	89.00	2.00	2.00
	10/20/15	167.30	-14.86	7.1	-119.2	-70.00	16.00	1.00	0.20	-84.00	14.00	1.10	0.30
	5/24/15	-175.96	-19.39	6.2	-135.7	81.00	26.00	0.90	0.50	84.00	29.00	0.90	0.60
	12/29/14	121.52	8.63	6.1	-68.1	80.00	18.00	1.20	0.70	81.00	41.00	1.20	1.70
	11/1/14	-177.76	-19.69	7.1	-134.2	-77.00	7.00	1.20	0.10	-88.00	11.00	1.20	0.20
	7/21/14	-178.40	-19.80	6.9	-133.7	-88.00	21.00	1.10	0.50	-77.00	25.00	1.20	0.70
TGTN	7/19/14	-174.45	-15.82	6.2	-135.8	-79.00	6.00	1.50	0.00	-81.00	5.00	1.40	0.20
	7/14/14	126.48	5.71	6.3	-73.8	61.00	25.00	0.60	0.40	62.00	35.00	0.60	0.60
	7/8/14	168.40	-17.69	6.2	-121.3	-71.00	28.00	0.60	0.50	-63.00	27.00	0.70	0.50
	7/3/14	-176.45	-30.46	6.3	-139.2	-82.00	25.00	1.00	0.50	-84.00	25.00	1.00	0.40
	5/4/14	179.09	-24.61	6.6	-133.3	-75.00	89.00	1.40	1.40	-76.00	40.00	1.40	1.40
WGLY	11/11/15	-72.01	-29.51	6.8	135.9	-15.00	18.00	1.30	0.50	-14.00	23.00	1.30	0.70

continued on next page

continued from previous page

	Event Info					RC				SC			
Station	Date	Lon (°)	Lat (°)	Mag	Φ (°)	ϕ (°)	σ_ϕ	δt (s)	$\sigma_{\delta t}$	ϕ (°)	σ_ϕ	δt (s)	$\sigma_{\delta t}$
	9/21/15	-71.38	-31.73	6.6	136.2	-10.00	34.00	0.70	0.70	3.00	35.00	0.70	0.60